Starch modified hyperbranched polyurethane/reduced graphene oxide-silver-reduced carbon dot nanocomposite

Highlight

The present work focuses on the *in situ* fabrication of hyperbranched polyurethane (HPU) nanocomposites with different weight percentages of reduced graphene oxide-silver-reduced carbon dot nanohybrid as nano-reinforcing material. The nanohybrid preparation was performed by a single one pot facile hydrothermal process. The nanohybrid and its nanocomposites were assessed by different analytical and spectroscopic techniques. HPU nanocomposite degraded 96% aniline, 95% ethyl paraoxon organophosphate and 93% rhodamine B upon exposure of sunlight for 4 h, 2 h and 1 h 10 min, respectively. These degradations followed the pseudo-first order kinetics model. The nanocomposite exhibited improvement in its performance in mechanical and thermal properties. They also displayed outstanding non-contact triggered shape-recovery upon exposure of microwave (99.8%) and sunlight (99.6%) within just 20 s and 60 s, respectively. Most significantly, they demonstrated efficient repeatable self-healing abilities under exposure of 20 s microwave (99.7%) power input (360 W), as well as under direct exposure of sunlight (99.5%) (10^5 lux intensity) for 4 min. Thus, the work forwards this multifaceted nanocomposite with photocatalytic activity as a potential high performing self-healing and self-cleaning material.

Parts of this chapter are published in

Duarah, R. and Karak, N. High performing smart hyperbranched polyurethane nanocomposites with efficient self-healing, self-cleaning and photocatalytic attributes. *New Journal of Chemistry*, 42(3):2167-2179, 2018.

6.1. Introduction

In recent times, bioinspired self-healing polymer(s) (SHP) and self-cleaning polymer(s) (SCP) attracted considerable interest as advanced engineering materials due to reduced energy consumption and minimal waste and resource. SHP can heal the minor damages caused by mechanical strain over time through triggering an autonomic healing process, whereas SCP maintain their surface free from contaminants and hence prolong the durability [1]. However, combining the attributes of self-healing, shape memory and self-cleaning into a single polymeric material still proves to be a daunting challenge owing to the structural incompatibility of hyperbranched polyurethane(s) (HPU). In shape memory polymer(s) (SMP), a permanent network structure is vital to restrict the chain motion and provide them with high modulus and stiffness. However, this proves to be contradictory to those of SHP where high chain mobility and inter-diffusion are essential [2]. Further, either a photocatalytic material or a super hydrophilic/super hydrophobic surface is essential in SCP for the removal of surface dirt [3].

In this context, polyurethane(s) (PU) are well-known SMP with unique attributes like wide transition temperature range of shape recovery, inherent soft-hard segments, high recoverable strain (up to 400%), etc. Further, HPU is three-dimensional globular like architecture with unique properties like higher functionality, solubility and reactivity, lower melt and solution viscosity and better compatibility with others including nanomaterials than their linear analogs [1]. Thus, starch modified biodegradable HPU may be an appropriate alternative to be used as such multifunctional smart material.

Further, structural stability and mechanical strength are the crucial attributes of smart HPU nanocomposites to meet the fundamental and practical importance. PU and poly(caprolactone) diol can secure the cracks above their melting temperature (T_m), but with a loss in dimensional stability of the material [4]. Huang *et al*. reported PU/graphene nanocomposite with multi-stimuli responsive self-healing behavior for repeated use but with poor mechanical properties [5]. This may be due to poor interactions between PU and graphene [6]. Therefore to achieve strong interactions with HPU, reduced graphene oxide (RGO) is found to be most suitable owing to its presence of optimal surface functional groups and easy mass production [7]. Moreover, RGO sheets also have excellent thermal conductivity, microwave (MW) and sunlight absorbing capacity [1]. Although, RGO may impart excellent mechanical and self-

healing properties, however, to accomplish attribute of self-cleaning and photocatalytic activity, additional suitable nanomaterials requires to be incorporated too. In this context, Ag not only enhances the photocatalytic activity due to its plasmonic activity but may also impart antimicrobial property [8, 9]. Again, reduced carbon dot (RCD), with its low band gap (3.1 eV) can absorb photons (UV) to produce electron-hole pairs (e^-/h^+) which react with O_2 and H_2O molecules to form hydroxyl radical ($^\bullet OH$) and superoxide radical ($^\bullet O_2^-$) as discussed in earlier chapter. These active radicals subsequently oxidize pollutants to CO_2 and H_2O [8, 10]. Thus, fabrication of a nanohybrid of RGO and RCD with Ag (RGO-Ag-RCD) may be attempted in order to reduce the optical band gap of the entire system and thereby enhancing its photocatalytic efficiency to different degrees depending on their intrinsic nature of e^- transportation and conducting ability. In addition, the polar surface functional groups in RCD and RGO can interact and adhere on the surface of the organic pollutants which assists in better degradation of the matter within a short degradation time.

Among different hazardous anthropogenic, pesticides and dyes are the most common non-degradable contaminants [10, 11]. In this regard, aniline is a carcinogenic chemical compound which causes tumors in animals and increases the risk of bladder cancer among humans [12]. It is worthwhile to make systematic efforts to degrade ethyl paraoxon organophosphate pesticide, aniline and rhodamine B using RGO-Ag-RCD nanohybrid under sunlight. The plasmonic property of Ag in the RGO-Ag-RCD nanohybrid can be utilized for the efficient capturing of solar light and thereby degrading such contaminants [8]. Therefore, an attempt was made to obtain a novel RGO-Ag-RCD nanohybrid using facile and eco-friendly hydrothermal technique. However, in order to improve the adsorption efficiency of the nanohybrid, it can be incorporated into the starch modified HPU to help in easy separation and recycling of the photocatalyst. This HPU nanocomposite is expected to impart combined attributes of enhanced mechanical performance, self-healing, self-cleaning and antimicrobial activity to the proposed bio-based smart HPU nanocomposite. To date, there is no reports on PU nanocomposites that feature SME, self-healing, self-cleaning properties and antimicrobial activity, altogether.

Therefore, an attempt was made to achieve the combined attributes of toughness, shape memory, self-healing and self-cleaning properties of the *in situ* fabricated starch modified HPU nanocomposites using different weight percentages of the RGO-Ag-RCD nanohybrid. Also, both nanocomposites and bare nanohybrid were used as photocatalysts for degradation of organic pollutants like aniline, ethyl paraoxon organophosphate and

rhodamine B under normal sunlight which is crucial for their further large scale practical applications.

6.2. Experimental

6.2.1. Materials

Polycaprolactone diol (PCL), toluene diisocyanate (TDI), 1,4-butanediol (BD), starch, ethanol and xylene of similar terms and grade were employed as described in **Chapter 2** (**Section 2.2.1**) and **Chapter 3** (**Section 3.2.1**). Tetrahydrofuran (THF, SD fine Chem., India) was vacuum-dried and stored with 4A-type molecular sieves, prior to use. Hyperbranched starch modified polyol (HBSP) was prepared using the same method as described in **Chapter 2** (**Section 2.2.3.1**). Silver nitrate ($AgNO_3$, Sigma Aldrich, Germany) was used as received. Graphene oxide (GO) was prepared by a modified Hummers' method [13]. Briefly, graphite powder (2 g) was added to 98% H_2SO_4 (35 mL) and stirred for 1 h on a magnetic stirrer. Subsequently, $KMnO_4$ (6 g) was added steadily into the above solution, below 20 °C. The mixture was then stirred at 35 °C in an oil bath for 4 h. To dilute the obtained solution, 90 mL of water was added by vigorous mixing for 1 h under stirring, following which a dark brown suspension was obtained. Further, 30% H_2O_2 solution was added drop wise to the suspension till the color of the solution changed to a bright yellow. Excess manganese salt from the resulting GO suspension was removed by centrifugation, continuous wash by 5% aqueous HCl solution, followed by H_2O, until neutral pH of the solution was achieved. Consequently, the obtained GO was dispersed in H_2O (0.5 mg mL^{-1}) and exfoliated ultrasonically, followed by centrifugation and vacuum drying in oven. *Citrus limon* (*C. limon*) fruits were purchased from the local market at Tezpur, India.

6.2.2. Methods

6.2.2.1. Preparation of RGO-Ag-RCD

Required amounts of GO (0.3 g) and $AgNO_3$ (0.3 g) were taken in 50 mL water. The mixture was stirred for 1 h and sonicated for 10 min to obtain a homogenous dispersion. Subsequently, an aqueous ethanolic solution of starch (3 g in 40 mL water and 25 mL ethanol) with a few drops of *C. Limon* extract was added to the homogenous dispersion of GO and $AgNO_3$ solution in an autoclave. The mixture was continuously heated for 5 h

at 150 °C. Consequently, the solution was cooled to room temperature followed by centrifugation at 10,000 rpm for 10 min. Finally, the nanohybrid was washed with distilled water and dispersed in it *via* sonication for 5 min.

6.2.2.2. Fabrication of HPU nanocomposites

PCL (6 g, 0.002 mol) and BD (0.36 g, 0.004 mol) were taken in a three necked round bottom flask, equipped with a mechanical stirrer and a nitrogen gas inlet. Consequently, TDI (0.007 mol, 1.22 g) was slowly added into the mixture at room temperature. The reaction mixture was stirred at (70 ± 2) °C for 3 h (maintaining -NCO/-OH ratio = 1). A viscous mass was obtained after the completion of the reaction which was considered as the pre-polymer. Subsequently, in the second step, HBSP (1.4 g, 0.01 mol) was added to the pre-polymer as the branch generating moiety, with the remaining amount of TDI (0.35 g, 0.002 mol) (maintaining -NCO/-OH = 1). Gradually, the temperature was raised to (80 ± 2) °C and continuously stirred for 2 h. Then the reaction was cooled down to room temperature. A dispersion of RGO-Ag-RCD nanohybrid in THF (0.5, 1 and 2 wt% with respect to HPU) was then added to the reaction mixture and the temperature was slowly elevated back to (80 ± 2) °C. The reaction was subsequently made to run for 2 h until its completion. HPU nanocomposites were obtained by performing three separate polymerization reactions with 0.5, 1 and 2 wt% of RGO-Ag-RCD, encoded as RNC0.5, RNC1 and RNC2, respectively. Pristine HPU was also prepared for comparison purposes without the incorporation of nanomaterial.

6.2.2.3. Shape memory study

To study the shape-memory behavior of HPU and its nanocomposites, strip samples were heated at 60 °C for 5 min and transformed into a spiral shape. Immediately, the spiral samples were immersed in an ice-water salt bath at -(15 ± 5) °C for 10 min to fix the temporary shape. The shape fixity of the cooled films was observed by drying them under vacuum followed by placing at room temperature (25 °C) for 30 min. Consequently, the fixed films were exposed to non-contact stimuli such as MW irradiation of 360 W for 20-30 s and under direct sunlight (11 am - 2 pm, at Tezpur University campus, altitude: 26.63 °N 92.8 °E in the month of June at sunny days, average temperature: 34 + 1 °C and humidity: 74 + 1%) under ambient condition. The shape recovery and the time required to retain original shape was noted. The shape recovery and shape fixity were calculated from the subsequent equations.

Shape recovery (%) = [(90-θ)/90] × 100 …….. (**Eq. 6.1**)

Shape fixity (%) = [θ/90] × 100 ……..... (**Eq. 6.2**)

where θ (degree) = Angle between the tangential line at the midpoint of the film and the line connecting the midpoint and the end of the curved film. The results are consistent as the test is repeated for five times.

6.2.2.4. Self-healing study

To determine the healing performance, films with a thickness of 0.5 mm of the nanocomposite were cut (10 mm x 0.2 mm x 0.015 mm in dimension) in a transverse direction by a razor blade, and the cracked was healed by sunlight or MW, separately. The optical images of the damaged, partially healed and completely healed films were captured by a polarising microscope. The healing efficiency was calculated as the ratio of the tensile strength values of the nanocomposites before and after healing. The tensile strengths of the pristine and the healed samples were measured by the same UTM. Samples were cut into strips of 80 mm x 10 mm x 0.50 mm for testing. The tensile strengths of pristine HPU, as well as the nanocomposites with different loadings of the nanohybrid were measured for at least four samples in each case, before and after the healing process. The optimal healing time for each case was defined as the shortest time required achieving the best healing efficiency under the given conditions. For MW healing, a domestic microwave oven (360 W) operating at a frequency of 2.45 GHz was used. Sunlight healing was performed under direct sunlight (11 am-2 pm) at Tezpur University campus (altitude: 26.631N 92.81E) in the month of November on sunny days [average temperature (29 ± 1 °C) and humidity (65 ± 1%)], with a light intensity of 90,000-100,000 lux.

6.2.2.5. Photocatalytic activity

Organic contaminant(s) (OC) like aniline, ethyl paraoxon organophosphate (pesticide) and rhodamine B (an organic dye) were used to study the photocatalytic degradation activity of RGO-Ag-RCD nanohybrid and HPU nanocomposite. In general, small pieces of HPU/RNC2 films (0.5 g) were placed independently into aqueous solutions (100 mL) of the pesticide (10 ppm), aniline (250 ppm) and rhodamine B (100 ppm). The solutions were stirred under normal sunlight (60000-80000 lux). The same experiment was also performed for nanohybrid with the equivalent amount of nanohybrid (0.01 g) for comparison purpose. The UV absorbance intensity at wavelengths of 548 nm, 271 nm

and 277 nm was determined to monitor the change in concentration of rhodamine B, pesticide and aniline, respectively at definite time intervals. The catalyst efficiency of the nanohybrid and the nanocomposite were determined from change of concentrations rates of the OC. The similar experiment was also done with same amount of nanohybrid under dark condition to confirm any possibility of adsorption. The experiment was also carried out without the presence of any nanomaterial under sunlight to determine the prospect of self-degradation. The amount of the degraded OC was obtained by the given equation [10].

$$\text{Degradation (\%)} = [(C_0\text{-}C)/C_0 \times 100] \quad \text{(Eq. 6.3)}$$

Where C_0 = initial concentration and C = concentration after photocatalytic degradation of the OC.

6.2.3. Characterization

RGO-Ag-RCD nanohybrid and HPU nanocomposites were characterized from Fourier-Transform Infrared (FTIR) spectroscopic and X-ray Diffraction (XRD) analyses by using the same instruments as mentioned in **Chapter 2** (**Section 2.2.2**). Raman and UV-visible analyses of the nanohybrid were conducted by using the same instrument as stated in **Chapter 3** (**Section 3.2.2**). The elemental analysis of the nanohybrid was done from Electron Dispersive X-ray (EDX) study by using the same instrument as described in **Chapter 3** (**Section 3.2.2**). Selected Area (Electron) Diffraction (SAED) pattern and the morphology of the nanohybrid and the nanocomposites were analyzed by the same High-Resolution Transmission Electron Microscopy (HRTEM) as mentioned in **Chapter 3** (**Section 3.2.2**). The characterization techniques for thermogravimetric Analysis (TGA), Differential Scanning Calorimetric (DSC), Universal Testing Machine (UTM) and impact resistance were same as mentioned in **Chapter 2** (**Section 2.2.2**). The optical images of the nanocomposite films during self-healing experiment were captured at 10X magnification by Motic polarising microscope (BA310Pol, China).

6.3. Results and discussion

6.3.1. Synthesis of RGO-Ag-RCD nanohybrid

The hydrothermal transformation of GO, Ag^+ and starch in presence of citric acid and ethanol at elevated temperature and pressure resulted a nanohybrid containing RGO, Ag

nanoparticle(s) (AgNP) and RCD. In the reaction system, Ag^{+} ion was converted to AgNP, GO was transformed to RGO and RCD was formed from starch and citric acid by the hydrothermal approach. This transformation is due to transfer of electron(s) e^{-} by the poly-phenolic mechanism as the components contain polar functional groups like carbonyl, hydroxyl, carboxylic and epoxy groups in their initial state as mentioned in **Sub-Chapter 4B**. The immediate e^{-} transfer reduction mechanism is presented schematically in **Scheme 6.1**.

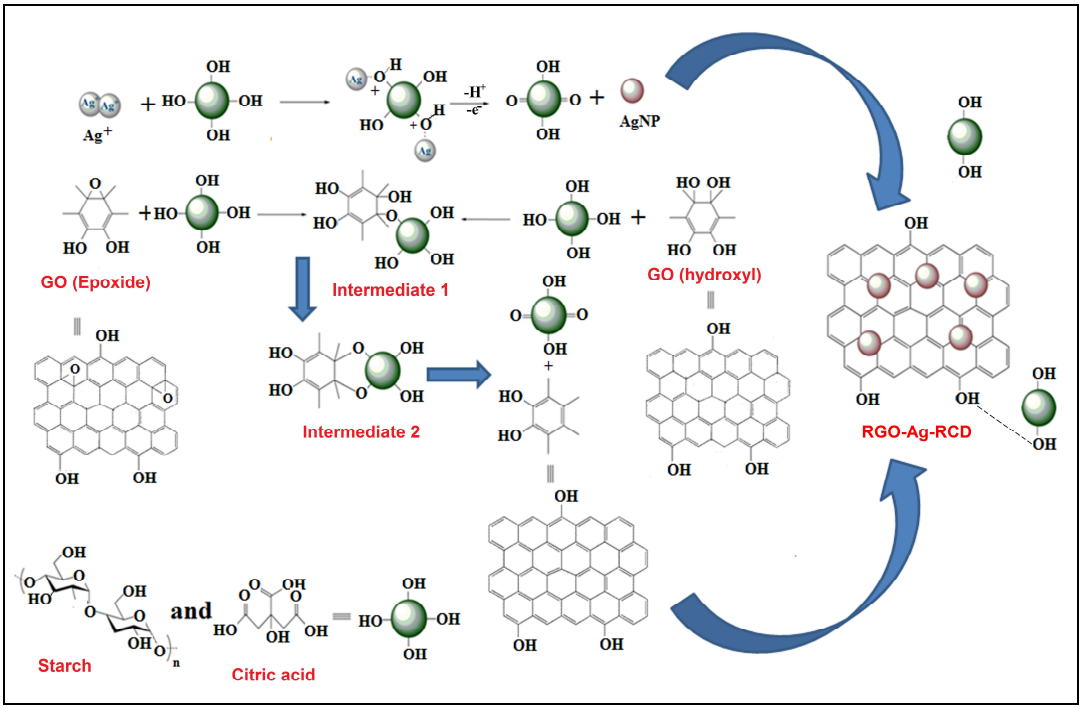

Scheme 6.1. Plausible electron transfer reduction mechanism for formation of RGO-Ag-RCD using starch and citric acid under hydrothermal treatment.

In this reduction process, RCD and RGO also serve as the capping agent. This is again ascribed to the optimum number polar peripheral groups on RCD and RGO [10]. It is important to mention that the reduction of Ag^{+} to Ag^{0} under the presence of GO and precursors of RCD cannot be entirely ruled out. The compositions of RCD precursors such as starch and lime extract have a plenty of carbohydrates, riboflavin, niacin, citric acid, thiamin, fats, etc. [14]. These biomolecules have a number of peripheral hydroxyl groups that primarily reduce Ag^{+} to Ag^{0} and transform themselves to corresponding carbonyl group as authenticated from FTIR results [15].

6.3.2. Characterization of RGO-Ag-RCD nanohybrid

FTIR spectra of GO and RGO-Ag-RCD are shown in the **Figure 6.1**. FTIR bands were observed at 1063 cm^{-1} (C-O stretching), 1261 cm^{-1} (C-O-C stretching), 1733 cm^{-1} (C=O stretching) and a broad band at around 3402 cm^{-1} (OH stretching). The presence of carbonyl, carboxylic and hydroxyl groups in GO, respectively [13]. Elimination of most of these oxygeneous groups of GO are clearly revealed by the absence or diminishing of intensity of the aforesaid bands in RGO-Ag-RCD [1, 13]. The relative intensity of the broad band for the hydroxyl group (at 3402 cm^{-1}) decreased due to the efficient reduction of GO [13].

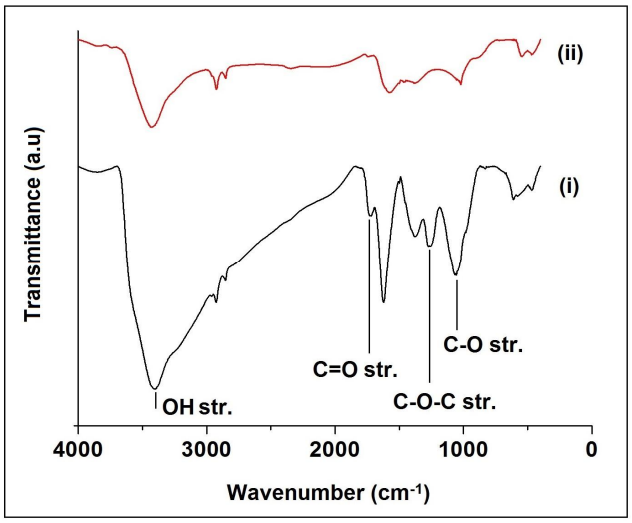

Figure 6.1. FTIR spectra of (i) GO and (ii) RGO-Ag-RCD.

The XRD patterns of the nanohybrid clearly showed the presence of AgNP in the system (**Figure 6.2**). RGO-Ag-RCD showed basal reflection peaks at 2θ = 38.4°, 44.2°, 64.4° and 74.3°, which correspond to (111), (200), (220) and (311) Braggs lattices of the fcc structure of silver (JCPDS 89-3722) [9]. The broad peak of RGO and RCD appeared at 23.2° corresponding to (002) plane of graphitic carbons [16]. This confirmed that AgNP and RCD were loaded onto the RGO sheets.

The actual content of the Ag phase was determined by EDX study) at two different points of the RGO-Ag-RCD nanohybrid. It was observed that there was 34 wt% and 30 wt% of Ag loaded on the nanohybrid with C/O ratio of 4.5 and 29, respectively, at two different points (**Figure 6.3a** and **b**). Both the C/O ratios were much higher than that of CD and GO [17]. This clearly indicates the elimination of oxygeneous groups in GO and CD.

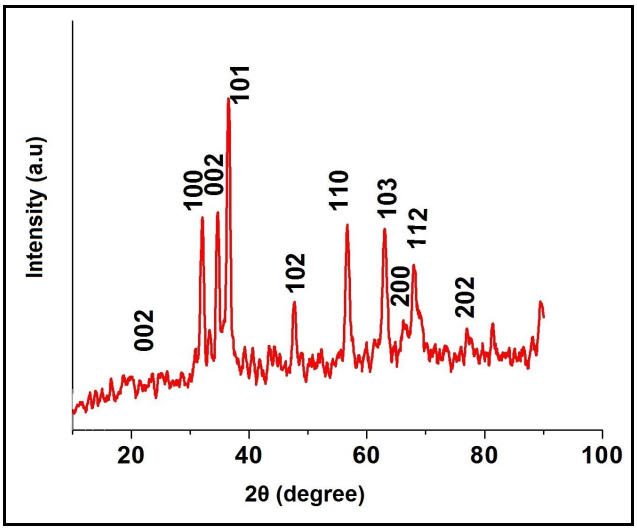

Figure 6.2. XRD pattern of RGO-Ag-RCD.

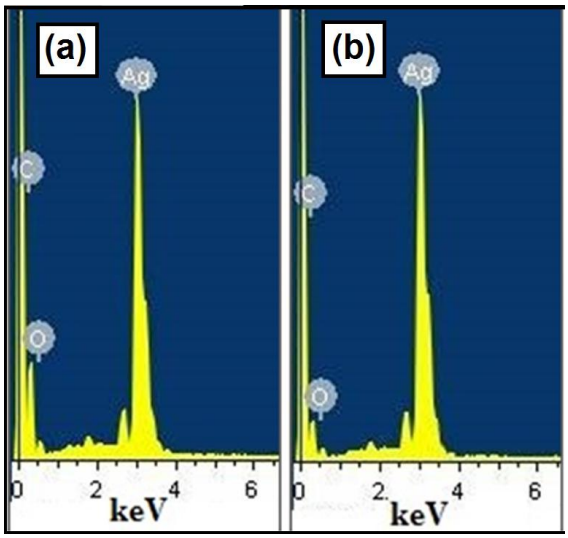

Figure 6.3. EDX maps of RGO-Ag-RCD at two different points **(a)** and **(b)**.

The Raman spectrum of RGO-Ag-RCD (**Figure 6.4**) with the characteristic D band (1360 cm^{-1}), G band (1592 cm^{-1}) and 2D band (2913 cm^{-1}) evidently indicated an increase in the I_D/I_G ratio on transformation of GO (1.14) to the nanohybrid (1.54) [18]. This is attributed to the decrease in the domain size of sp^2 carbon and its restoration upon reduction of GO. Also the unrepaired defects that remained even after the elimination of some of the oxygeneous groups resulted in the multilayer graphitization of RGO-Ag-RCD [18, 19]. Moreover, the variation in the I_D/I_G is also attributed to the fact that AgNPs and RCD are impregnated on the RGO sheets, which enhanced the I_D band intensity.

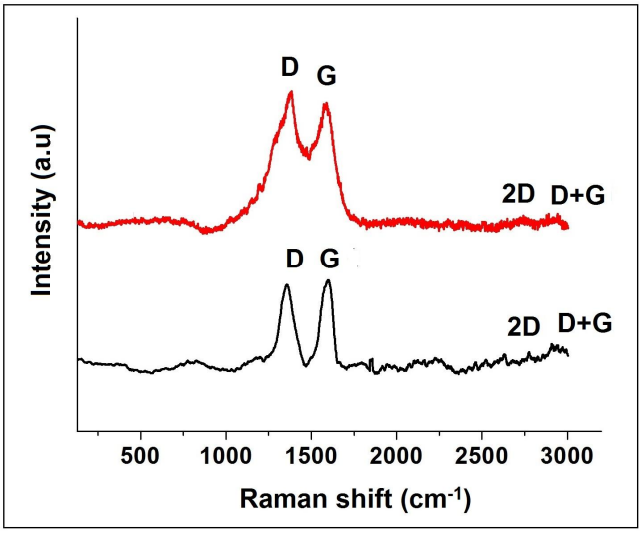

Figure 6.4. Raman spectra of (i) GO and (ii) RGO-Ag-RCD.

The HRTEM images of RGO-Ag-RCD nanohybrid (**Figure 6.5**) confirm the creation of almost spherical RCD and AgNPs embedded on the RGO sheets. They were held by means of strong interactive forces that stabilize each other mutually.

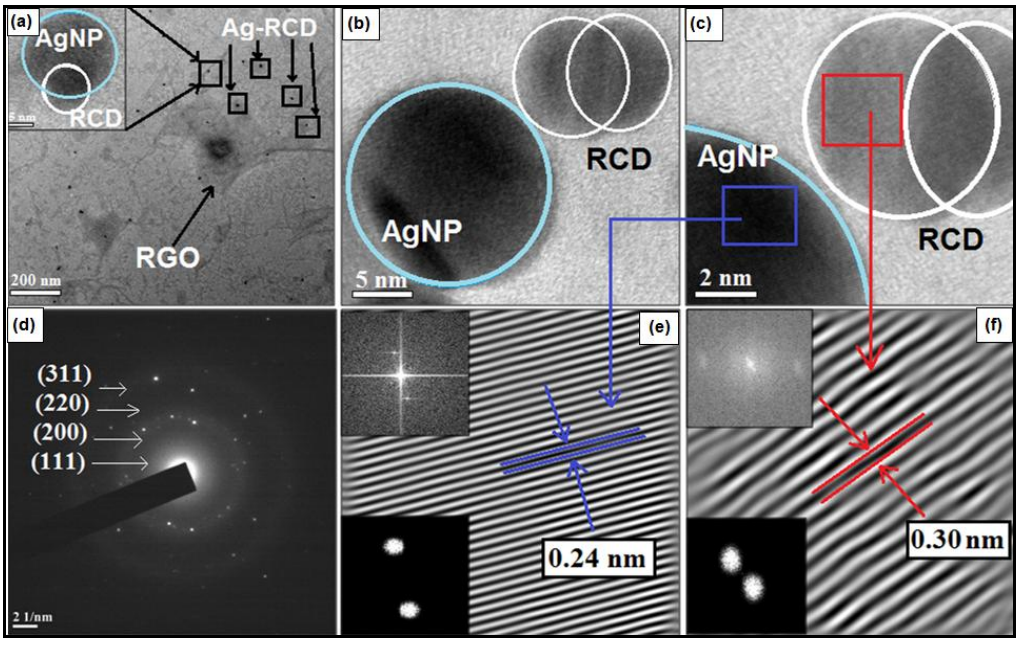

Figure 6.5. HRTEM images at magnifications **(a)** 0.2 µm of RGO-Ag-RCD nanohybrid (with AgNP (blue circle) and RCD (white circle) at 5 nm as inset); **(b)** 5 nm, **(c)** 2 nm magnification of AgNP and RCD, **(d)** SAED pattern of RGO-Ag-RCD nanohybrid, FFT images of RGO-Ag-RCD phase **(e)** before masking and after masking (at inset); and **(f)** IFFT of RGO-Ag-RCD phase showing the lattice fringes.

The diameter of AgNP and RCD were observed to be in the range of 10-15 nm and 2-3 nm with lattice fringe spacing of 0.240 nm and 0.30 nm, respectively. Ag^{+} ions and RCD form complexes with the -OH and C=O peripheral polar functional groups of GO and other precursors prior reduction and convert to Ag^{0} on the sheets after reduction. This confirmed the *in situ* formation of RCD, RGO and AgNPs simultaneously. Further, the UV-visible spectrum (showed later) of RGO-Ag-RCD nanohybrid shows the red shift of AgNP which confirms the bigger size of AgNP in the nanohybrid. The formation of a crystalline structure of RGO-Ag-RCD nanohybrid is also clearly indicated by a well-defined fcc crystal lattice of 0.240 nm for (111) plane of AgNP as obtained from the IFFT image (showing the lattice fringes), and SAED pattern (**Figure 6.5**) [9, 20].

6.3.3. Fabrication of HPU nanocomposites

The HPU nanocomposites were fabricated by an *in situ* polymerization technique (**Scheme 6.2**) [1, 13].

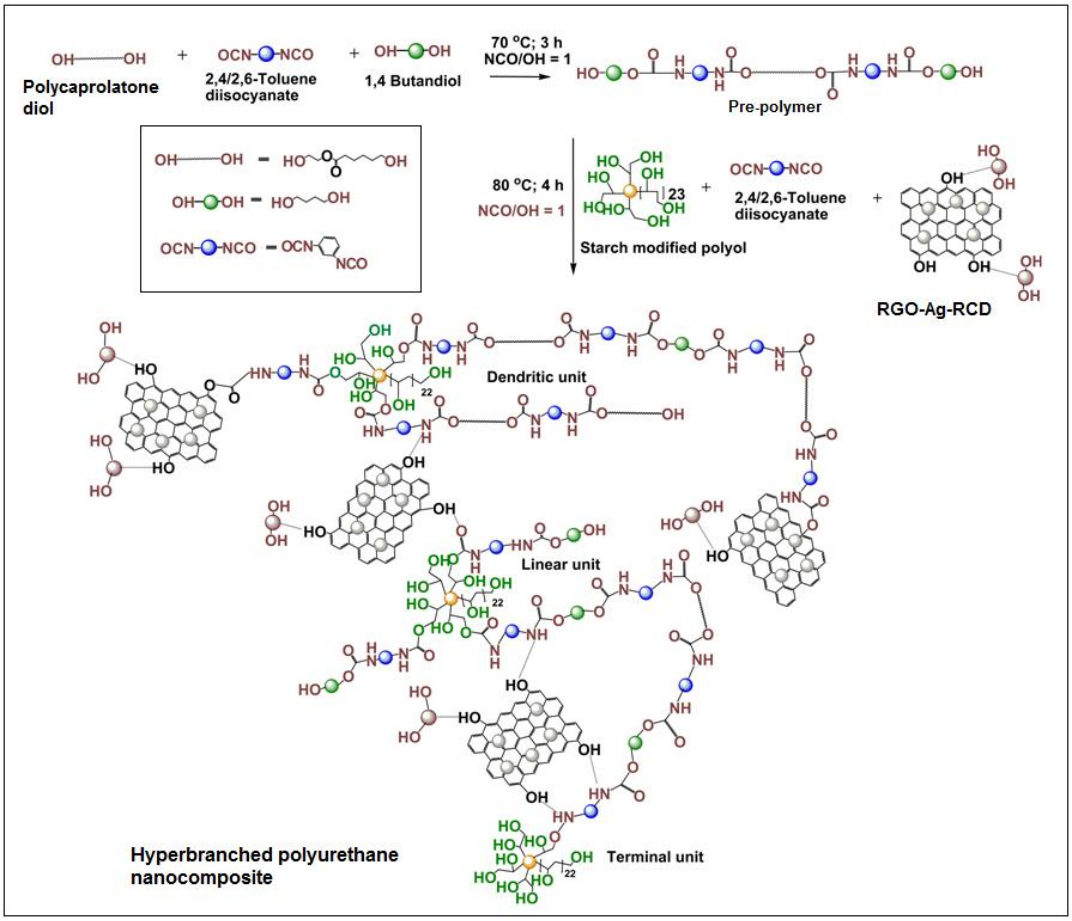

Scheme 6.2. Route for formation of HPU nanocomposite.

Concentration of the reactants, nature and amount of nanohybrid, rate of addition of the branching moiety, temperature and reaction time are the primary aspects for the successful nanocomposite preparation [21]. Consequently, branching unit was added drop-wise at room temperature in a dilute xylene solution (15-20%) to avoid gel formation, in the second step of the reaction. Also, the nanohybrid was gradually incorporated in the second step to achieve strong interfacial interactions with the HPU matrix that result in better stabilization of nanohybrid within the matrix [13, 21].

6.3.4. Characterization of HPU nanocomposites

Figure 6.6a shows the FTIR spectra for HPU nanocomposites where an important modification was observed in the region 1731-1686 cm^{-1}. HPU showed a single band at 1731 cm^{-1}, but was split into two in case of the nanocomposites [22].

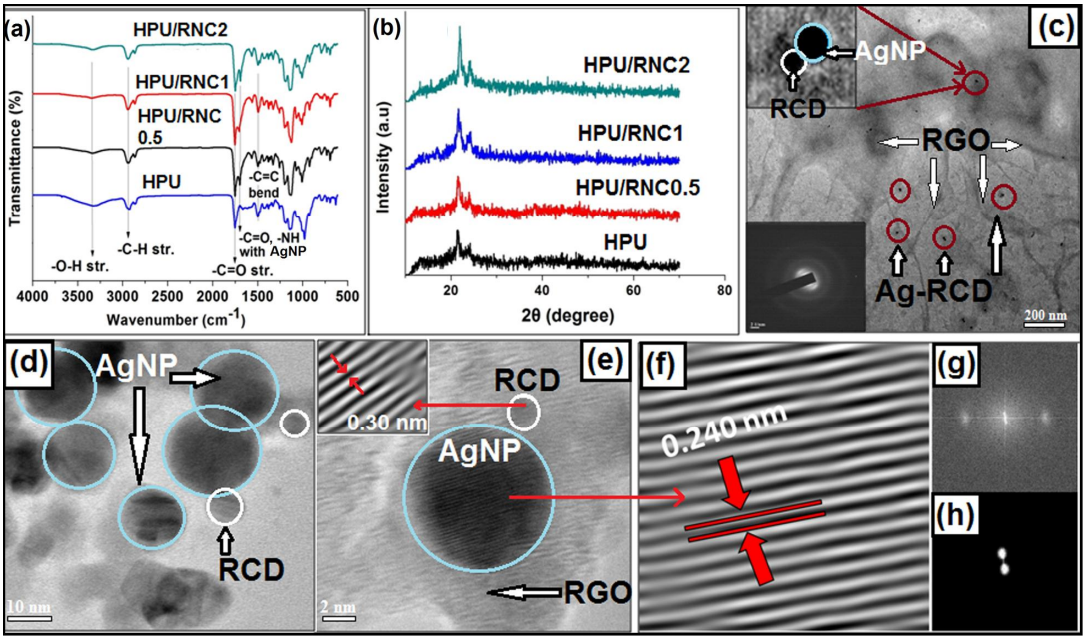

Figure 6.6. (a) FTIR spectra, **(b)** XRD patterns of HPU and its nanocomposites; HRTEM images at magnifications of **(c)** 0.2 µm, **(d)** 5 nm and SAED pattern (at inset), and **(e)** 2 nm; **(f)** IFFT of RGO-Ag-RCD showing lattice fringes of Ag, and FFT of RGO-Ag-RCD (g) before masking and **(h)** after masking.

The bands near 1617 cm^{-1} are typically due to H-bonding interactions of the -NH and -C=O groups with the surface charge of AgNP [22]. Additionally, the band at 1731 cm^{-1} for HPU/RNC2 appears to be less intense as compared to others due to greater wt% of

the nanohybrid. This is, further, supported by the shift of -NH absorption band from 3466 cm^{-1} to 3454 cm^{-1}. Moreover, the disappearance of the isocyanate band near 2270 cm^{-1} clearly signifies the absence of free isocyanate in the system [1, 13, 21]. The XRD patterns (**Figure 6.6b**) of HPU and its nanocomposites displayed two different peaks at $2\theta = 21.2°$ (*d* spacing = 0.407 nm) and 23.3° (*d* spacing = 0.371 nm) due to (110) and (200) credited to the PCL crystals [1, 21]. After nanohybrid incorporation, the PCL peaks shifted towards a more intense and higher angle that is attributed to the formation of a denser structure in contrast to the pristine HPU. This suggests that crystallinity of the nanocomposites increased with increase in the amount of nanohybrid which acts as a nucleating agent. Nevertheless, no characteristic peak was observed for AgNP in the XRD patterns of the nanocomposites due to the presence of very minute quantity of AgNP present in the system. Moreover, the HRTEM images of HPU/RNC2 (**Figure 6.6c** to **h**) confirmed homogenous dispersion of the respective nanomaterial within the HPU matrix. Further the presence of Ag and RCD in RGO sheets is also confirmed by measuring the fringes with inter-planar spacing of 0.24 nm and 0.30 nm, respectively, same as the bare RGO-Ag-RCD (**Figure 6.5**).

6.3.5. Optical properties

The UV-visible spectroscopy extended the clear evidence of the reduction of $AgNO_3$ and GO (**Figure 6.7a**). GO showed peaks at 228 nm and 302 nm which are due to the π-π* and n-π* transition of the aromatic C=C and C=O bonds respectively [17, 23]. A red shift was observed for the first peak near 264 nm which specifies the restoration of the electronic conjugation by the formation of RGO and RCD with a more graphitic structure in the UV-visible spectrum of RGO-Ag-RCD nanohybrid [24]. The SPR band of AgNPs was observed near 430 nm in the UV-visible spectrum of RGO-Ag-RCD nanohybrid. This demonstrates that the particle size increases as it is generated in situ where Ag^+ ion forms complexes with OH and C=O groups of RGO, RCD and other precursors present in the system [25]. The optical band gaps of RGO-Ag-RCD nanohybrid, RGO, RCD and AgNP were calculated from UV-visible spectra (**Figure 6.7a**) by using the following equation.

$$\alpha = C(h\nu - E_{bulk})^{1/2}/h\nu \quad \text{(Eq. 6.4)}$$

Where α = absorption coefficient, C = constant, h = plank's constant, ν = frequency and E_{bulk} = bulk 'band gap'. The band gaps were obtained by extrapolating a linear regression at $(\alpha h\nu)^2 = 0$ of the plot $h\nu$ versus $(\alpha h\nu)$ [17]. The optical band gaps of individual

nanomaterials mainly RGO (3.68 eV), AgNP (4.33 eV) and RCD (3.1 eV) were found to be much higher than that of the nanohybrid (2.78 eV) obtained by combining them (**Figure 6.7b** to **d**). This may be due to *in situ* formation of the nanohybrid by simultaneous reduction of GO, CD and Ag ions by a single pot one step process. In other words, the result of band gap indicates the formation of a new nanohybrid with unique interfacial structure.

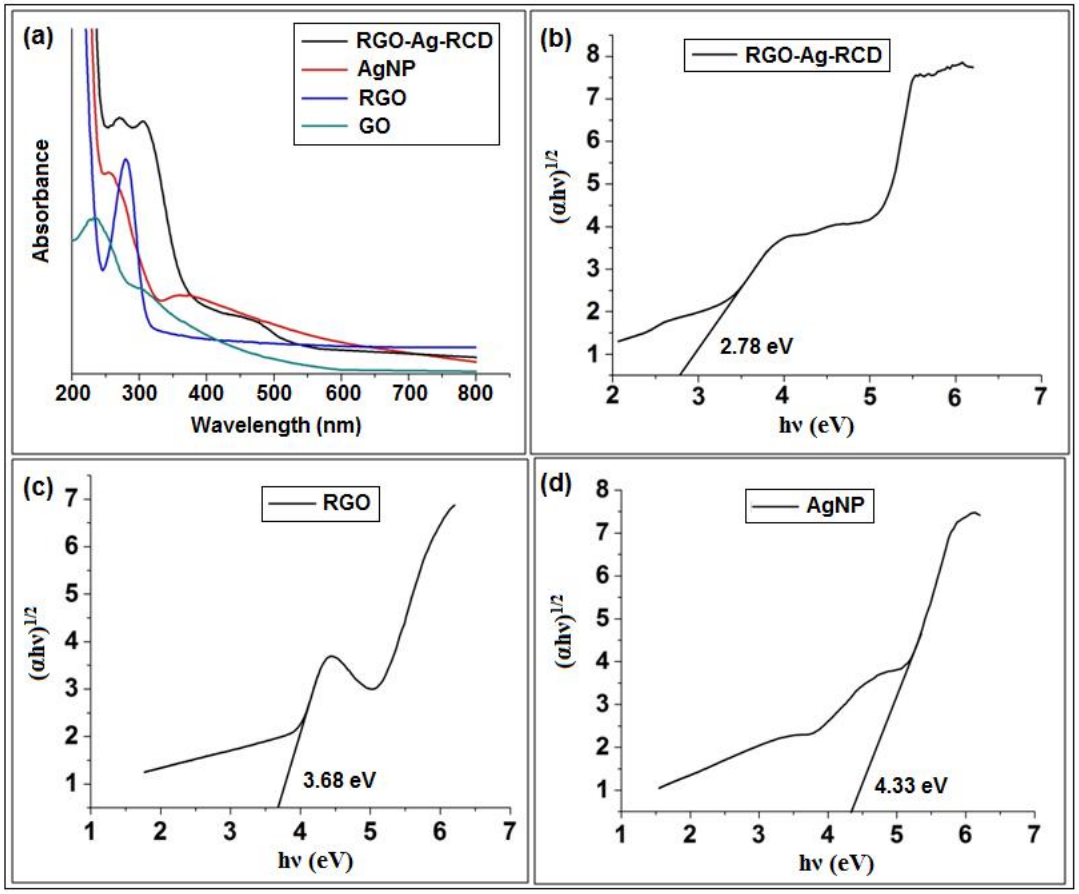

Figure 6.7. (a) UV-visible spectra of (i) RGO-Ag-RCD (ii) AgNP (iii) RGO (iv) GO; (αhν)1/2 vs hν plots of **(b)** RGO-Ag-RCD, **(c)** RGO and **(d)** AgNP.

This result of band gap clearly demonstrated the requirement for fabrication of the nanohybrid which can efficiently create e^-/h^+ pairs and thereby helping in photocatalytic transformation reaction. The band gaps of the hydrothermally synthesized RGO and AgNP agree with the earlier reported values for them [17]. This reduced band gap suggests that the synthesized RGO-Ag-RCD has significant impact on the absorption of solar light.

6.3.6. Mechanical properties

Mechanical properties of HPU and its nanocomposites are tabulated in **Table 6.1.** After incorporation of the RGO-Ag-RCD nanohybrid, all the nanocomposites exhibited excellent dose-dependent mechanical properties (**Figure 6.8)**. One evident achievement of this study is the simultaneous improvement of tensile strength and elongation at break, which resulted in a high toughness for the nanocomposite.

Table 6.1. Mechanical properties of HPU and its nanocomposites

Property	**HPU**	**HPU/ RNC0.5**	**HPU/ RNC1**	**HPU/ RNC2**
Tensile strength (MPa)	17.6 ± 1.2	23.2 ± 1.4	28.7 ± 1.6	34.7 ± 1.5
Elongation at break (%)	1158 ± 15.2	1180 ± 16.4	1311 ± 18.1	1363 ± 19.2
Scratch hardness (kg)	6.5 ± 0.2	>10	>10	>10
Impact strength[a] (kJ m^{-1})	>19.02	>19.02	>19.02	>19.02
Toughness[b] (MJ m^{-3})	136.7 ± 10.3	217.3 ± 15.2	350.35 ± 16.5	405.42 ± 12.8

[a]*Maximum limit of the instrument.*

[b]*Calculated by integrating the area under stress-strain curves.*

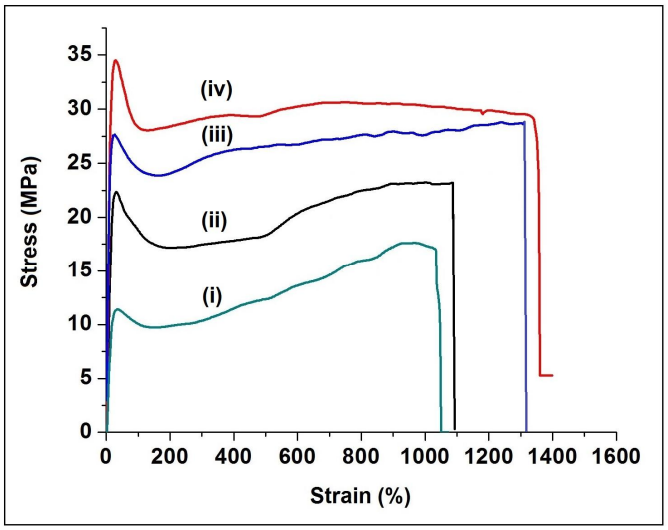

Figure 6.8. Stress-strain profiles of (i) HPU (ii) HPU/RNC0.5, (iii) HPU/RNC1 and (iv) HPU/RNC2.

The improved performance of the nanocomposites can be attributed to good compatibility between HPU and the nanohybrid, excellent dispersion and strong interfacial interaction of the nanohybrid with the HPU matrix [1, 21]. Furthermore, the polar peripheral groups of nanohybrid with aromatized core structure stiffen the hard domain and provide strong interactions by virtue of H-bonds, non-covalent and covalent bonds with the polymer chains. These strong chemical bonds assist to attain a successful transfer of the load from HPU to the nanohybrid in the HPU nanocomposite [26]. This consequently enhances the tensile modulus of the nanocomposite with increase in the content of nanohybrid. Further, the nanocomposites also exhibited outstanding flexibility with very high elongation at break with increase in the content of nanohybrid. As cited in literature, such an enhancement is attributed to the alignment of polymer chains in the initial stage of tensile loading, which forces them to orient the nanohybrid along the direction of loading [13]. At higher stress, RGO layers slide past each other since they are strongly bound to the adjacent HPU chains through multiple secondary interactions. This further helps to overcome the π-π stacking interactions between the RGO sheets. As RGO favorably enhanced the hard segment in comparison to the soft segment, a typical stiffness of the soft segment was evaded [27]. In nutshell, the combined effect resulted in the enhancement of the overall elongation of the nanocomposites. Further, scratch hardness was enhanced with the incorporation of nanohybrid into the HPU matrix. Also, the HPU nanocomposites showed the highest limit (used instrument) of impact energy owing to the presence of soft segments in the polymer chain, which dissipates the impact energy. Thus, in general mechanical performance of HPU/RNC2 was found to be superior among the studied nanocomposites. This highlights the suitability of the former for different advanced applications.

6.3.7. Thermal properties

TGA thermograms of HPU nanocomposites are shown in **Figure 6.9a** and **b**. The nanocomposites established a two-step degradation patterns owing to the presence of both hard and soft segments in the HPU matrix. This implies that the nature and loading of the RGO-Ag-RCD nanohybrid do not considerably control the degradation pattern of the nanocomposites. All the nanocomposites revealed higher thermal stability as compared to HPU (**Table 6.2**).

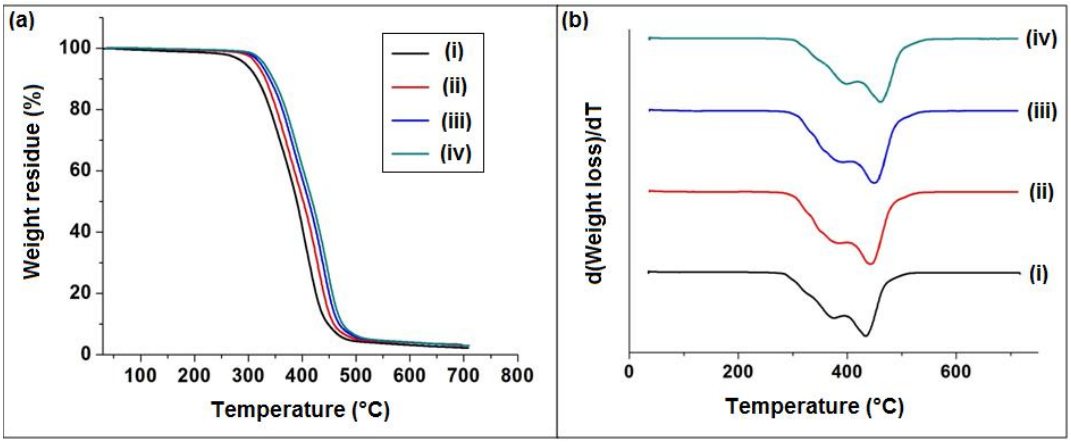

Figure 6.9. (a) TGA thermograms and **(b)** DTG curves of (i) HPU (ii) HPU/RNC0.5, (iii) HPU/RNC1 and (iv) HPU/RNC2.

Nevertheless, the nanocomposites displayed improved thermal stability by increase in the loading of nanohybrid in comparison to HPU (**Table 6.2**). This is attributed to good dispersibility of RGO-Ag-RCD nanohybrid in the HPU matrix and the presence of AgNP. The nanohybrid acts as the heat stabilizer and efficiently limits the movement of the HPU chains [28]. Further, RGO-Ag-RCD contributes in the physical cross-linking process by virtue of functional groups. These consequences in effective restrictions in the HPU chain motions and make the degradation process energy consuming. Consequently it offers in superior thermo-stability to the nanocomposites as compared to HPU [1, 29].

Table 6.2. Thermal properties of HPU and its nanocomposites

Property	**HPU**	**HPU/ RNC0.5**	**HPU/ RNC1**	**HPU/ RNC2**
Peak temperature (1st stage degradation) (°C)	371	383	388	392
Peak temperature (2nd stage degradation) (°C)	436	442	449	452
Weight residue (%)	3.4	3.5	3.6	3.8
Melting temperature (T_m, °C)	40.2	44.6	49.6	53.8
Melting enthalpy (ΔH_m, J g^{-1})	43.4	47.5	52.3	57.3

On exposure to thermal energy, the chain excitation and molecular motion are generated which are greatly prohibited due to the secondary interactions of nanohybrid with the HPU chains [1]. The improved barrier property of the HPU nanocomposites also assist to retain the volatiles produced throughout decomposition process in the HPU matrix [28, 29]. Additionally the thermal stabilities of the nanocomposites are also enhanced due to the strong hydrogen bond, non-covalent and covalent interactions between the HPU matrix and nanohybrid.

DSC analyses were conducted to explore the melting temperature (T_m), melting enthalpy (ΔH_m) and crystallization behavior of HPU nanocomposite (**Figure 6.10**).

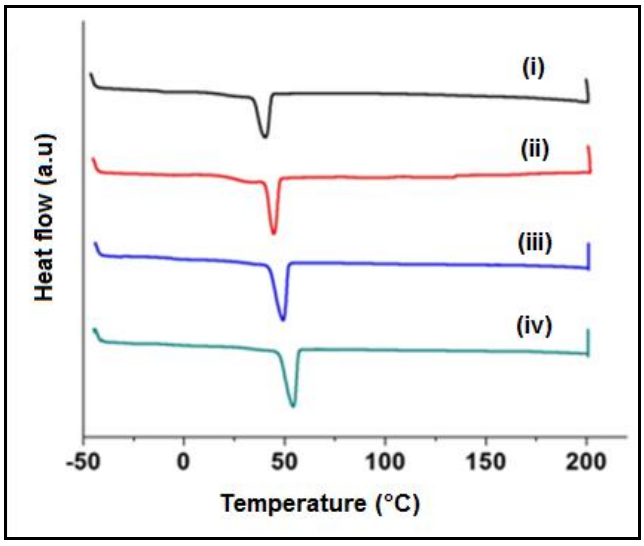

Figure 6.10. DSC curves of (i) HPU (ii) HPU/RNC0.5, (iii) HPU/RNC1 and (iv) HPU/RNC2.

The T_m of the soft segment was noticeably dependent on the RGO-Ag-RCD nanohybrid amount and moved to higher temperature on increase in the nanohybrid content (Table 6.2). The presence of nanohybrid forced the arrangement of the HPU molecular chains and thus improves the T_m of the HPU nanocomposites [29]. The enhancement of crystallinity can also be predicted from the ΔH_m values as given in Table 6.2. Significant literatures cite the improvement of crystallinity of a semi crystalline polymer with the incorporation of various nanomaterial [28, 29]. This undoubtedly specifies that the homogenously distributed nanohybrid offers as the nucleating agent and enhances the crystallization process through arrangement of the soft segment in a particular direction [30].

6.3.8. Shape memory study

The non-contact triggered shape memory behaviors of the nanocomposite under exposure of MW and sunlight are shown in **Figure 6.11**. All the nanocomposites exhibited exceptional shape fixity and recovery under the mentioned stimuli.

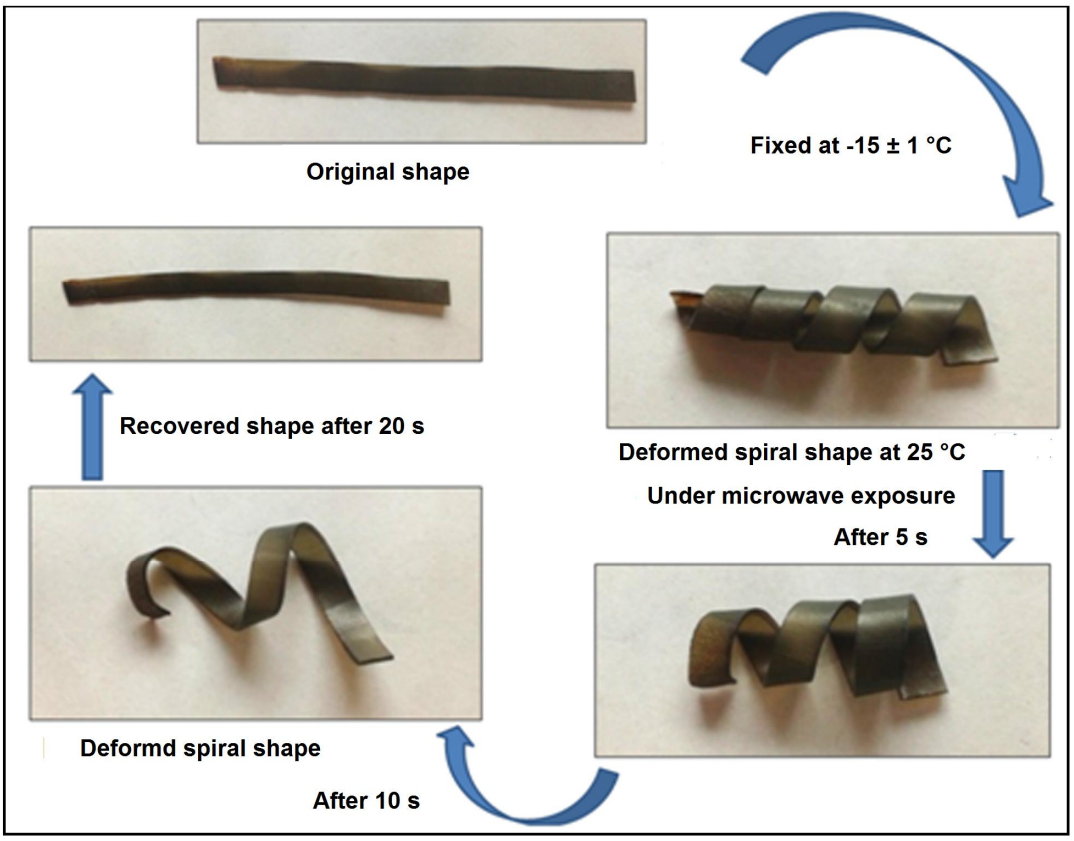

Figure 6.11. Shape memory behaviors of HPU/RNC2 under microwave.

This may be due to excellent MW and sunlight absorbing capacity of RGO. Shape recovery time and ratio under different stimuli are tabulated in **Table 6.3**. In the permanent shapes of the HPU nanocomposite and pristine HPU films, the polymeric chains are oriented in a random coil arrangement *i.e.*, at their maximum entropic state [31]. Upon heating the nanocomposite films, chain mobility is activated due to which they can be easily given temporary spiral shape. Consequently, the spirally shaped films were quenched in an ice salt bath at -(15 ± 5) °C for 5 min. The kinetic freezing of the polymer's molecular chains fixes the temporary spiral shape which minimizes their entropic state. At this stage, the polymeric chains did not have sufficient energy to reverse the deformation. Subsequently, upon reheating the films under sunlight and MW,

the molecular chain mobility was reactivated which allowed the chains to gain entropy and return to the random coil motion [1, 21]. The shape recovery of the HPU nanocomposites was found to be enhanced with the increase in wt% of nanohybrid (**Table 6.3**). The HPU/RNC2 film exhibited the highest shape recovery among the nanocomposites.

Table 6.3. Shape memory properties of HPU and its nanocomposites

Stimulus	Property	HPU	HPU/ RNC0.5	HPU/ RNC1	HPU/ RNC2
Sunlight	Shape recovery (%)	98.7 ± 0.1	99.4 ± 0.2	98.6 ± 0.1	99.8 ± 0.2
	Shape fixity (%)	98.6 ± 0.1	99.2 ± 0.2	99.2 ± 0.3	99.4 ± 0.2
	Shape recovery time (s)	120 ± 0.1	60 ± 0.1	60 ± 0.1	60 ± 0.1
Microwave	Shape recovery (%)	90 ± 0.3	99.2 ± 0.1	99.4 ± 0.1	99.6 ± 0.2
	Shape fixity (%)	92 ± 0.2	99 ± 0.1	99.4 ± 0.2	99.6 ± 0.2
	Shape recovery (s)	60 s	20 s	20 s	20 s

Better shape recovery of HPU nanocomposites as compared to HPU is due to the increased stored energy of system. This is due to multifunctional moiety hyperbranched polyol, homogeneous distribution of hard segments, increased secondary interactions in the structure of HPU matrix and homogenization of reinforcing nanomaterial [1]. There was an increased stored energy of the homogeneously distributed RGO-Ag-RCD nanohybrid. This enhanced the interaction between the hard segment of HPU and nanohybrid, through generation of strong net points [1, 13]. The RGO-Ag-RCD nanohybrid assists the nanocomposites to attain a high recovery stress attributed to the release of the stored elastic strain [13, 31]. The shape recoveries of the nanocomposites were found to be improved with an increase in nanohybrid amount in the matrix, which associates the improved degree of crystallinity (**Table 6.2**) [1]. RGO and RCD created a huge amount of stored elastic strain energy due to the presence of strong interfacial

interactions with the HPU matrix. Also, the enhancement of the MW and sunlight absorbing capacity with the increase of the nanohybrid content is another chief factor for fast recovery. Thus, by deformation of such heat sensitive SMPs above their T_m, a desired shape can be attained which can be sustained after cooling. Such non-contact triggered SMP nanocomposite can have potential advanced applications.

6.3.9. Self-healing study

The self-healing capability of the nanocomposites was examined by optical imaging and tensile strength measurement. The fracture of the nanocomposite was effectively healed by exposure to direct sunlight and MW (**Figure 6.12**). The optical images prior to and after the healing process evidently reveal the complete healing of the nanocomposite film. The healing efficiency of the nanocomposites under sunlight and MW clearly depends on the loading of RGO-Ag-RCD and exposure time.

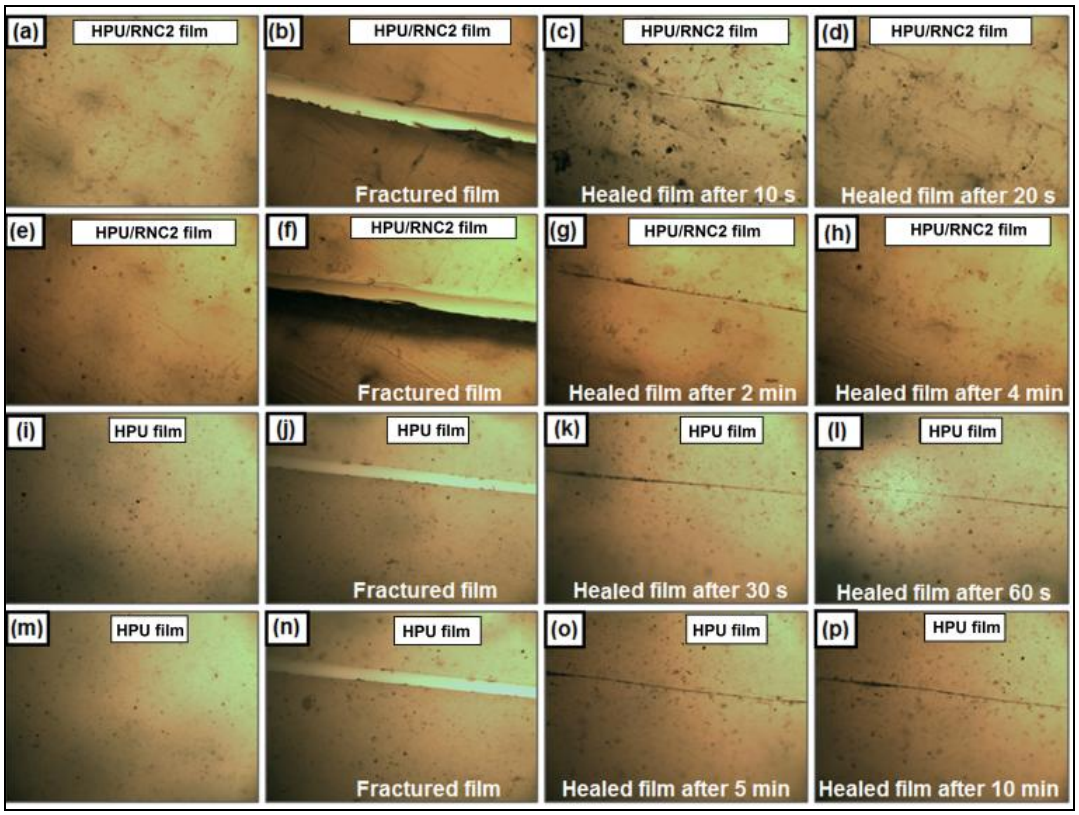

Figure 6.12. Optical microscopic images showing self-healing of HPU/RNC2 **(a)-(d)** under microwave, **(e)-(h)** under sunlight; and optical microscopic images showing self-healing of HPU **(i)-(l)** under microwave and **(m)-(p)** under sunlight.

All the nanocomposites were healed rapidly with outstanding healing capability after the integration of a minute amount (0.5-2 wt %) of RGO-Ag-RCD nanohybrid. These HPU nanocomposites were effectively healed within 20 s under low MW power (360 W) and within 4 min under direct sunlight with a high healing efficiency of 99.7% and 99.5%, respectively (**Figure 6.13**), respectively. Here, it is pertinent to mention that pristine HPU only slightly healed (10-15)% after 30 s of MW exposure whereas HPU/RNC2 completely healed within 20 s at a MW power input of 360 W. Also, pristine HPU underwent only (10-12)% healing after 10 min of sunlight irradiation. The intrinsic properties like excellent MW and sunlight absorbing capacity with high thermal conductivity of the nanohybrid help in the healing process [1]. During the healing process, the absorbed MW energy by nanohybrid results in oscillating its dipoles, and generates heat at the nanohybrid-polymer interface due to friction.

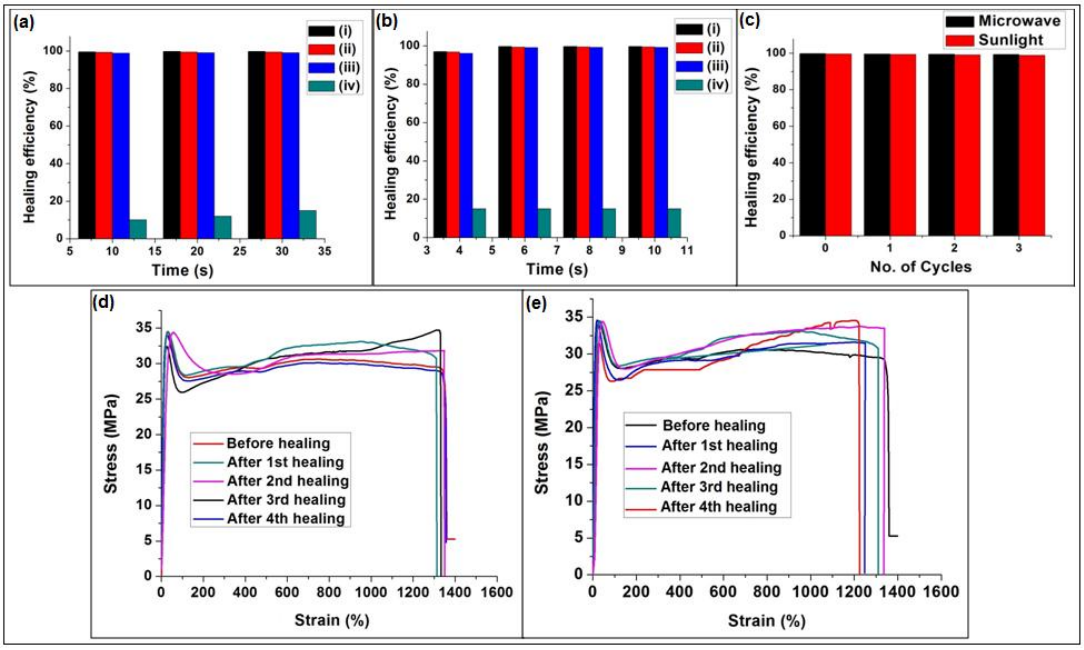

Figure 6.13. (a) The healing efficiency of (i) HPU/RNC2, (ii) HPU/RNC1, (iii) HPU/RNC0.5 and (iv) HPU under microwave power 360 W at different times; **(b)** The healing efficiency of (i) HPU/RNC0.5, (ii) HPU/RNC1, (iii) HPU/RNC2 and (iv) HPU under sunlight at different times; **(c)** Healing efficiency of HPU/RNC2 under microwave and sunlight at 20 s and 4 min, respectively, for repeated cycles; Stress-strain profiles of HPU/RNC2, before and after healing with different repeating cycles, under **(d)** microwave and **(e)** sunlight.

The nanohybrid efficiently transfers this absorbed energy to the HPU matrix which aids in melting of the soft segment as its T_m is around 60 °C and initiates molecular diffusion (Brownian movement) of the segment towards the crack. Similar to MW, the solar energy is efficiently transferred throughout the nanocomposite and assists the rapid Brownian movement of the molecular chains of the segment (**Scheme 6.3**).

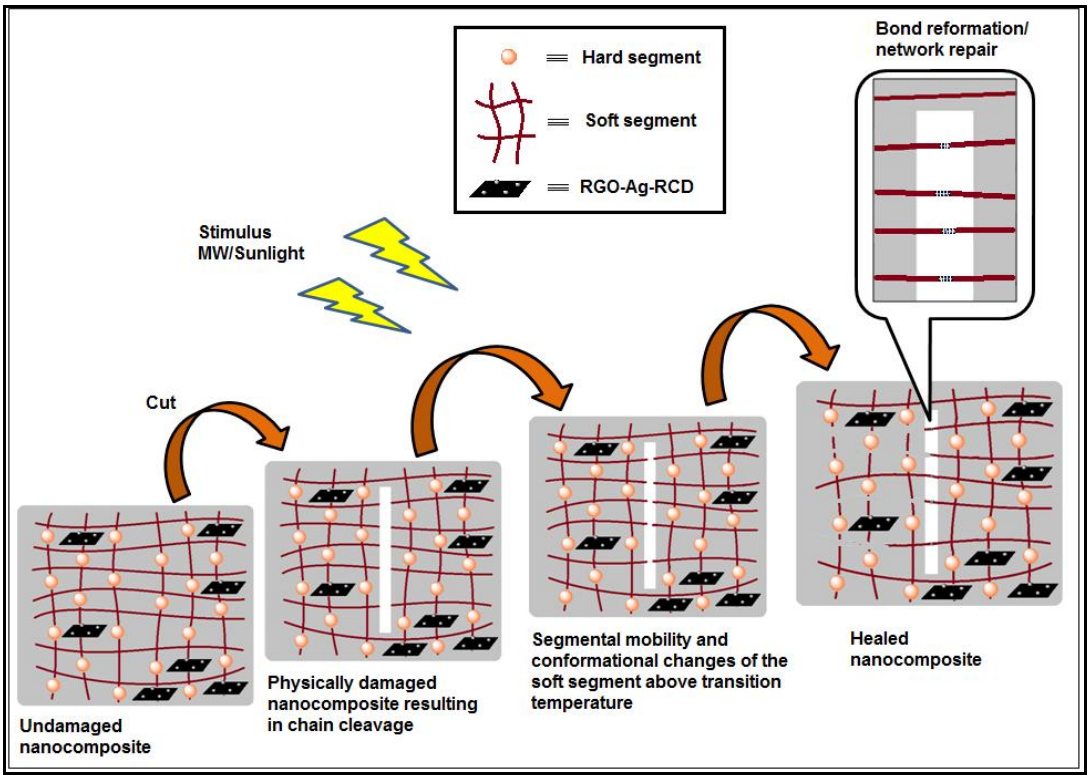

Scheme 6.3 Cartoon representative mechanism for self-healing of the HPU nanocomposite.

As self-healing was achieved by the rearrangement and diffusion of the soft segments of HPU, it leads to permanent repair of the cracked site, which can be repeated for multiple times [31]. Meanwhile, the hard segment of HPU helps to retain the sample dimensions [32]. The study also revealed that the used energy of the stimulus was insufficient to cause any dimensional instability or degradation, as confirmed by TGA analysis of HPU nanocomposites. Suitable variation of the composition of the nanohybrid plays a vital role in attaining the desired self-healing capability. The nanocomposite with 1% and 2% of nanohybrid demonstrated rapid healing within 4 min, with excellent healing efficiency under direct sunlight exposure. In spite of molecular restrictions, the HPU/RNC2 nanocomposite demonstrated better healing efficiency compared to the other studied

nanocomposites. This is due to the presence of a higher amount of nanohybrid in it, which helps to absorb more MW/solar energy and transfer this energy to the HPU matrix for rapid healing with remarkable healing efficiency [31]. However, it is pertinent to mention that HPU exhibited a SME but not self-healing ability, although both the processes depend on the rearrangement of the polymeric chains. This is attributed to the fact that the energy necessary for activation of the polymeric chain in order to rearrange its orientation and attain its original shape is less in comparison to the diffusion of polymeric chains at the damaged surface [1]. The polar functional groups of pristine HPU can absorb a definite amount of energy from the stimulus to rearrange and revert back to their original (permanent) shape from the deformed state (temporary shape). Nevertheless, this amount of energy is not adequate for the diffusion of polymeric chains due to which pristine HPU only demonstrate SME [18, 32]. On the other hand, RGO-Ag-RCD nanohybrid has a better ability to absorb energy from MW and sunlight due to which it absorbs and transfers more amount of energy to the HPU matrix of the nanocomposite. The soft segment of HPU melts in the nanocomposite and diffuses in the cracked places, and thus heals it. Again, repeated healing is a daunting challenge to the material scientist and important for the self-healing materials. This could greatly increase the service lifetime. In this work, as self-healing was achieved by the rearrangement of soft segments of HPU with the assistance of the SME, the healing of the prepared nanocomposites could be repeated again and again. Thus, even after the fourth cycle of the experiment, the healing ability of the nanocomposite remains almost same under both sunlight and MW (**Figure 6.13c**). Representative stress-strain curves for before and after healing with different repeating cycles are shown in **Figure 6.13d** and **e**.

6.3.10. Photocatalytic activity

A probable mechanism (**Scheme 6.4**) of solar light assisted photocatalytic degradation has been proposed which consider AgNP and RCD as antennae for solar light and RGO for efficient e^-/h^+ separation. Nanoparticle-based photocatalysis requires efficient capture of solar light, generation of e^-/h^+ pairs and effective use of e^-, h^+ or both before they are recombined [33]. However, the excitation recombination lifetime for a semiconductor nanoparticle is normally on the picoseconds scale [34]. Consequently, rapid excitation recombination leads to inefficient photocatalytic reactions. Herein, RGO-Ag-RCD nanohybrid was primarily selected for two motives. First, AgNPs can be utilized to capture solar light, with reduction in the effective band gap of RGO and AgNP. And

second, RGO-Ag-RCD can delay the recombination of e^-/h^+ pair of RGO which allows effective charge separation and photocatalytic activity [8]. Most significantly, the electrostatic interaction between cationic AgNP and anionic RGO and RCD leads to strong interaction among them which enhances the above factors.

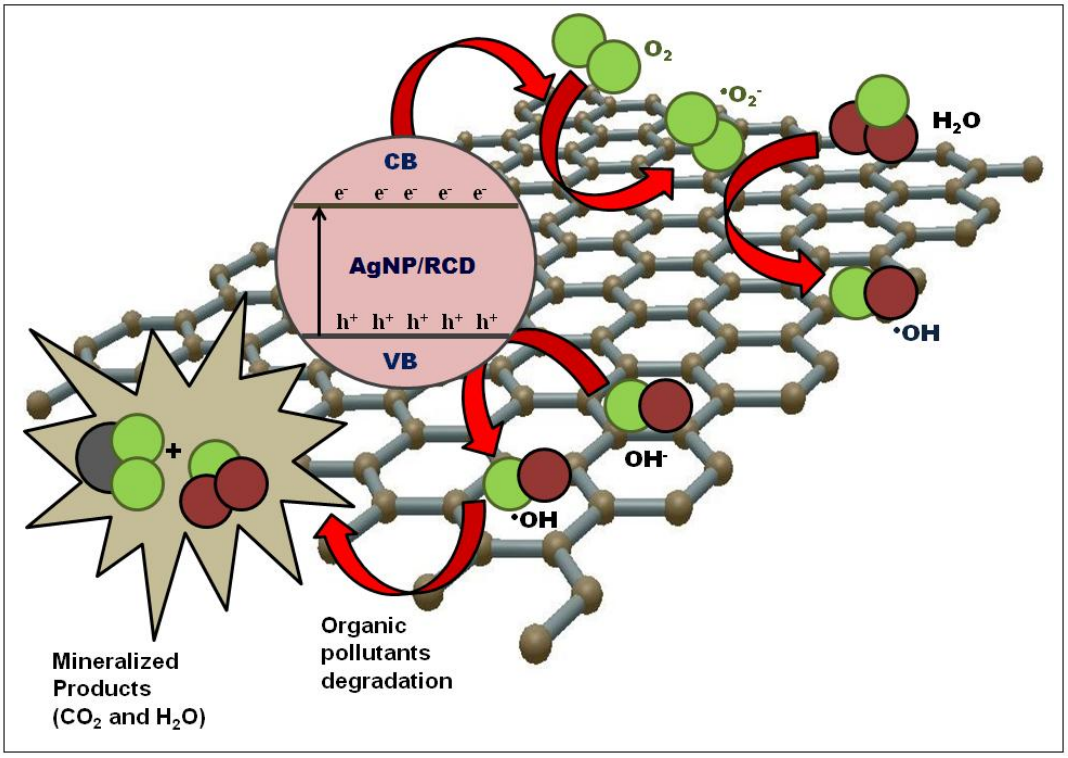

Scheme 6.4. Photocatalytic degradation mechanism by HPU nanocomposite.

The electrostatic force among RCD, RGO and AgNP provides tunneling of photo-excited e^- which is utilized for photodegradation of OC [35]. Moreover, the presence of polar peripheral functional groups and high surface area of the nanohybrid makes it accessible to the OC. Indeed the nanohybrid was found to be very effective solar light assisted photocatalyst for degradation of aniline, ethyl paraoxon organophosphate and rhodamine B. Solar light excites the AgNP surface plasmon and this coherent oscillation of e^- produces high concentration of energetic e^- on their surface. The π-conjugated RGO and RCD surface adjacent to the AgNPs rapidly transports the e^- via its extended π-conjugation structure and leads to the efficient separation of e^-/h^+ pairs. The phenomenon of e^- transfer is basically possible because of the low band gap of nanohybrid (2.78 eV). The e^- can react with dissolved O_2 to generate reactive oxidative species ($^{\bullet}O^{2-}$, O_2^{2-}), whereas the h^+ on AgNP may react with H_2O molecules to produce $^{\bullet}OH$ radicals. These

oxidative species degrade the organic molecules by an oxidative pathway as discussed in **Sub-Chapter 4B**. Previous studies report the degradation of organic molecules into small molecules with few intermediates [8]. The concentration changes of the OC with time clearly demonstrated the effective degradation of the contaminants as measured by UV absorbance **(Figure 6.14)**.

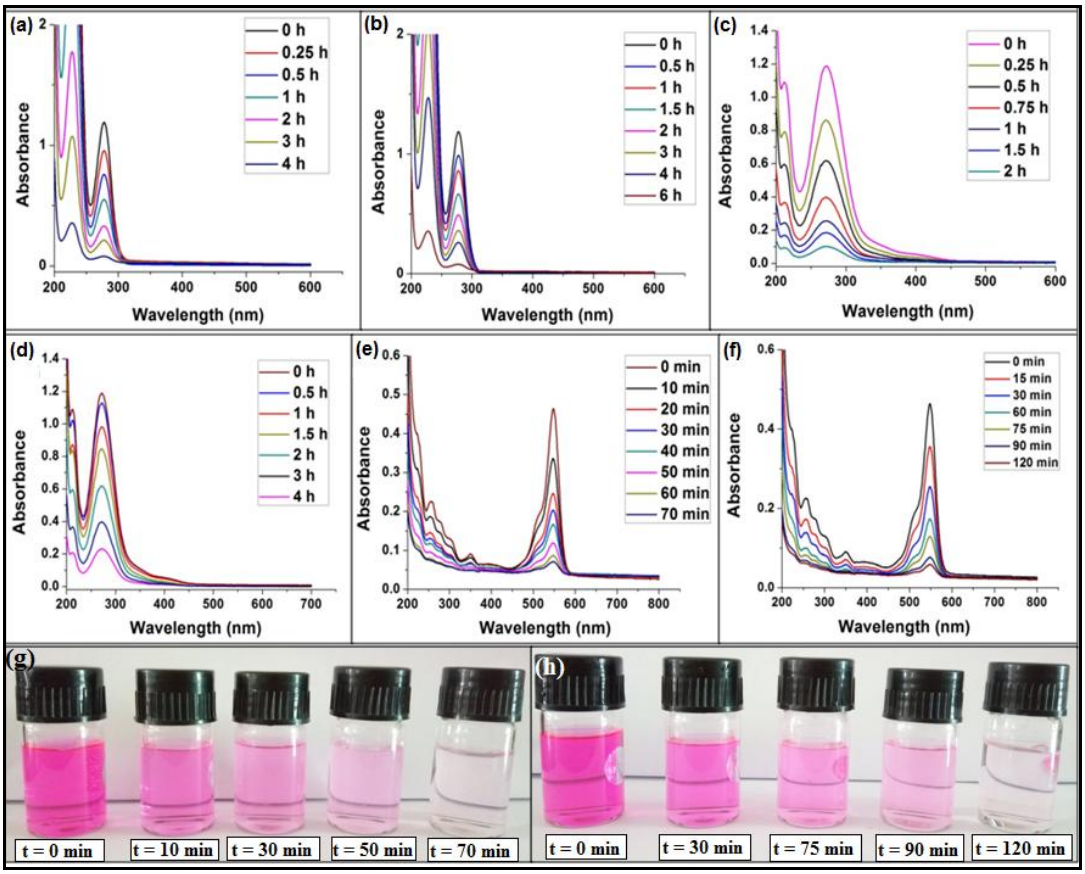

Figure 6.14. Plots of UV absorbance against wavelength at different times for the degradation of aniline in the presence of **(a)** HPU/RNC2, **(b)** RGO-Ag-RCD; of ethyl paraoxon organophosphate in the presence of **(c)** HPU/RNC2, **(d)** RGO-Ag-RCD; of rhodamine B in the presence of **(e)** HPU/RNC2 **(f)** RGO-Ag-RCD; and Images showing the degradation of rhodamine B by **(g)** HPU/RNC2 and **(h)** RGO-Ag-RCD at different times under sunlight.

The plots of optical absorbance against wavelength for the degradation of OC at different times for both HPU/RNC2 and RGO-Ag-RCD are shown in **Figure 6.14**. Literature reports that 0.15 g of ZnO nanoparticles can degrade 95% rhodamine B at 10 ppm concentration under 70 min of UV irradiation [11]. Conversely, 0.5 g of HPU/RNC2

nanocomposite film can degrade 93% of rhodamine B under 70 min of solar light irradiation. Again, Pirasaheb *et al*. reported that 0.5 g of immobilized Cr:ZnO nanoparticles can degrade 93% of aniline at pH 9, under 6 h of sunlight irradiation [35]. On the other hand, 0.5 g of HPU/RNC2 nanocomposite film can degrade 96% degradation of the aniline under 4 h of solar light irradiation. Again De *et al*. reported 90% degradation of ethyl paraoxon organophosphate using 0.15 g carbon dot reduced Cu_2O hyperbranched epoxy nanocomposite under 5 h of solar light irradiation [10]. However, 0.5 g of HPU/RNC2 nanocomposite film showed 95% degradation of ethyl paraoxon organophosphate in just 2 h of sunlight irradiation. The pseudo-first order kinetic model equation was used to describe the photo-degradation behavior of nanocomposite films as follows [10].

$$-dC/dt = K_1t \quad \text{(Eq. 6.5)}$$

where C is the concentration of pollutants at any time t and K_1 is the apparent rate constant. After integrating equation (v), the following equation is obtained.

$$\ln(C/C_0) = -K_1t \quad \text{(Eq. 6.6)}$$

where C_0 is the initial concentration (at t = 0) of the OC. The fitting plots of $\ln(C/C_0)$ versus time (**Figure 6.15**) demonstrate the degradation of the OC is well described by pseudo-first order kinetics with the fitting coefficients over 0.9, indicating a regular photo-degradation behavior. Also, to examine the effect of superiority of HPU/RNC2 nanocomposite compared to its nanohybrid, the dye degradation using nanohybrid was also tested (**Figure 6.15**). It was observed that 0.01 g of RGO-Ag-RCD nanohybrid required 6 h, 4 h and 2 h of sunlight irradiation for 93%, 80% and 86% degradation of aniline, pesticide and rhodamine B, respectively. The results clearly indicated the superiority of the HPU nanocomposite over the nanohybrid. The various polar functional groups of HPU may interact with the polar groups of the OC which help to adhere on their surfaces and facilitate the interaction with the active oxygen radicals [10]. Therefore, the nanocomposite film has enhanced catalytic efficiency due to the strong interaction between the nanohybrid and the HPU matrix and the prevented leaching of the materials. Also, photocatalytic degradation of the OC was performed under dark condition with RGO-Ag-RCD nanohybrid. It was observed that even after 6h of sunlight irradiation, the intensity measurement by UV-visible spectroscopy indicates no decrease of intensity (**Figure 6.15**). Thus, this result eliminates the possibility of adsorption of organic molecules by the nanomaterial. Additional experiments were also designed for self-degradation of the OC without using any nanomaterial under sunlight. The

measurement of their intensities after 6 h by UV-visible spectroscopy clearly indicates that organic contaminant degradation was not self-degradation (**Figure 6.15**).

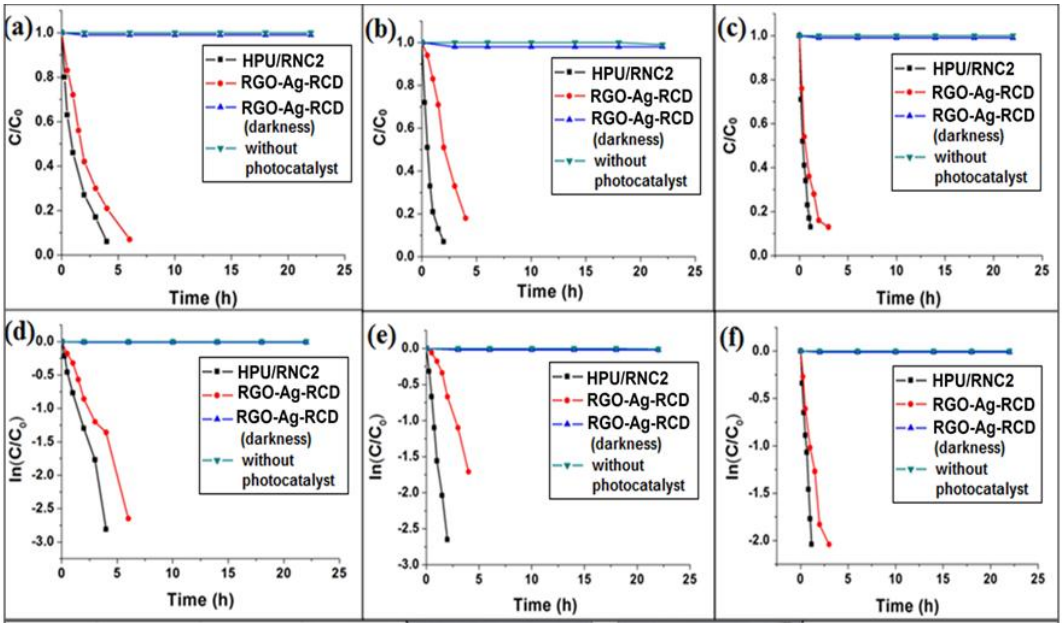

Figure 6.15. Degradation curves of aqueous solutions of **(a)** aniline, **(b)** ethyl paraoxon organophosphate and **(c)** rhodamine B using HPU/RNC2and RGO-Ag-RCD; and fitting degradation kinetic curves for **(d)** aniline, **(e)** ethyl paraoxon organophosphate and **(f)** rhodamine B using HPU/RNC2and RGO-Ag-RCD.

There was no color change in the rhodamine B solution even after 6 h exposure under sunlight as shown in **Figure 6.16a**. For the same reasons as stated above, HPU nanocomposite demonstrated the self-cleaning property by degradation of rhodamine B as model dirt on Al plate coated films under sunlight irradiation by visual means as shown in **Figure 6.16b**. Only the plate coated with the HPU nanocomposite could decolorize the dye. For a better comparison, Al plate coated with pristine HPU was dipped in aqueous solution of dye and exposed to sunlight. Upon exposure, the changes in color of the films were recorded at different times as shown in **Figure 6.16**. The photographs illustrate that the nanocomposite exhibits better decolorization of the model dirt over a period of 70 min in comparison to HPU. Thus, it can be utilized as a material for designing of self-cleaning surface. However, it is pertinent to mention that, the recovery of the nanohybrid catalyst is difficult because of its nano-level dispersion in water by the strong interactions of polar functional groups of RCD and RGO.

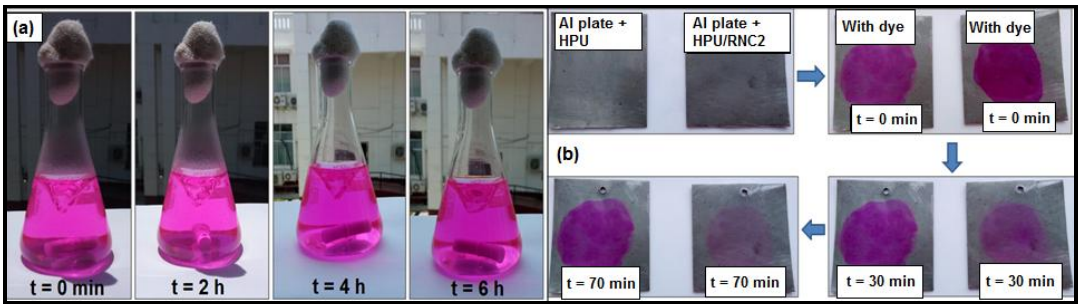

Figure 6.16. (a) Rhodamine B solution without nanomaterial under sunlight at different times and (b) images showing the decolorization of rhodamine B by Al plates coated with HPU/RNC2.

The catalyst recovery requires a large amount of solvent, as well as high speed of centrifugation (8000-10,000 rpm) process and hence its reuse is not effective. On the other hand, the nanocomposite film (finely chopped) can be easily recovered from the reaction medium (water) and hence can be effectively recycled. The recyclability of solar light assisted photocatalytic performance of the HPU/RNC2 catalyst has been investigated for aniline degradation (**Figure 6.17**).

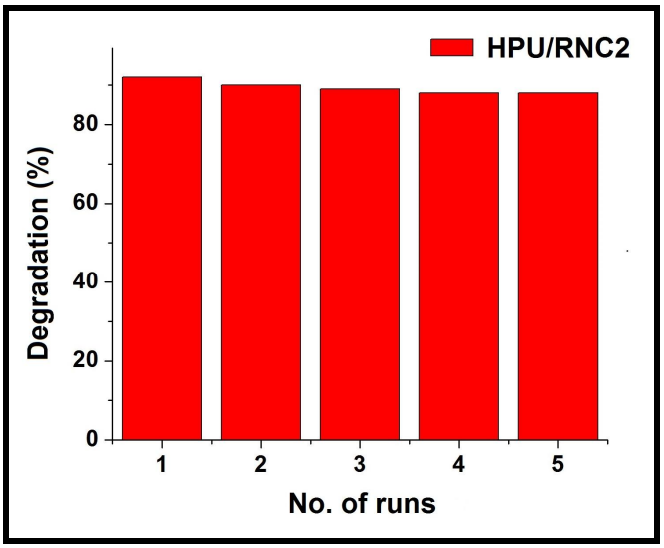

Figure 6.17. Photocatalytic degradation of aniline using recycled HPU/RNC2 five consecutive times.

It was observed that even after five consecutive recycling of HPU/RNC2, there was no significant decrease in its photocatalytic efficiency. The products formed at the end of the photocatalytic degradation of the pesticide are CO_2, H_2O, O_2, N_2, and phosphoric

acid [10]. The potential end products for the aniline and rhodamine B degradation are CO_2 and H_2O [11, 35].

6.4. Conclusion

Pioneering functionalization of reduced graphene oxide-silver-reduced carbon dot nanohybrid (RGO-Ag-RCD) was accomplished by a green one-pot single step hydrothermal approach. Moreover, reduction of optical band gap was possible through this unique approach. Again, in situ fabrication of starch modified hyperbranched polyurethane reduced carbon dot-reduced graphene oxide-silver nanocomposite resulted high performing smart solar light assisted photocatalyst for effective degradation of different organic pollutants. Tuning of mechanical, thermal, self-healing and shape memory behaviors can be achieved by judicious choice of fabrication process and loading of RGO-Ag-RCD in the nanocomposites. Outstanding shape recovery (>99%) of the nanocomposite under microwave and sunlight, along with rapid and repeatable efficient self-healing under the same stimuli were achieved rhodamine B under solar light irradiation. Thus, the simultaneous demonstration of such attractive attributes by the same material justifies the prospects of employing the fabricated nanocomposite for the development of recyclable solar light assisted photocatalyst that could resolve environmental and ecological problems as well as overcome the limitations associated with the preparation of high performing material simultaneously. The nanocomposite also demonstrated excellent photocatalytic efficiency for the degradation of aniline, ethyl paraoxon organophosphate and rhodamine B under solar light irradiation. Thus, the simultaneous demonstration of such attractive attributes by the same material justifies the prospects of employing the fabricated nanocomposite for the development of recyclable solar light assisted photocatalyst that could resolve environmental and ecological problems as well as overcome the limitations associated with the preparation of high performing material.

References

[1] Thakur, S. and Karak, N. Tuning of sunlight-induced self-cleaning and self-healing attributes of an elastomeric nanocomposite by judicious compositional variation of the TiO_2-reduced graphene oxide nanohybrid. *Journal of Materials Chemistry A*, 3(23):12334-12342, 2015.

[2] Jochum, F. D. and Theato, P. Temperature- and light-responsive smart polymer materials. *Chemical Society Reviews*, 42(17):7468-7483, 2013.

[3] Tobaldi, D. M., Ferreira, R. A. S., Pullar, R. C., Seabra, M. P., Carlos, L. D., and Labrincha, J. A. Nano-titania doped with europium and neodymium showing simultaneous photoluminescent and photocatalytic behavior. *Journal of Materials Chemistry C*, 3(19):4970-4986, 2015.

[4] Sun, L., Huang, W. M., Lu, H., Lim, K. J., Zhou, Y., Wang, T. X., and Gao, X. Y. Heating-responsive shape-memory effect in thermoplastic polyurethanes with low melt-flow index. *Macromolecular Chemistry and Physics*, 215(24):2430-2436, 2014.

[5] Huang, L., Yi, N., Wu, Y., Zhang, Y., Zhang, Q., Huang, Y., Ma, Y., and Chen, Y. Multichannel and repeatable self-Healing of mechanical enhanced graphene-thermoplastic polyurethane composites. *Advanced Materials*, 25(15):2224-2228, 2013.

[6] Park, J. and Yan, M. Covalent functionalization of graphene with reactive intermediates. *Accounts of Chemical Research,* 46(1):181-189, 2013.

[7] Zhou, Y., Bao, Q., Tang, L. A. L., Zhong, Y., and Loh, K. P. Hydrothermal dehydration for the "green" reduction of exfoliated graphene oxide to graphene and demonstration of tunable optical limiting properties. *Chemistry of Materials*, 21(13):2950-2956, 2009.

[8] Bhunia, S. K. and Jana, N. R. Reduced graphene oxide-silver nanoparticle composite as visible light photocatalyst for degradation of colorless endocrine disruptors. *ACS Applied Materials & Interfaces*, 6(22):20085-20092, 2014.

[9] Barua, S., Thakur, S., Aidew, L., Buragohain, A. K., Chattopadhyay, P., and Karak. N. One step preparation of a biocompatible, antimicrobial reduced graphene oxide-silver nanohybrid as a topical antimicrobial agent. *RSC Advances*, 4(19):9777-9783, 2014.

[10] De, B., Voit, B., and Karak, N. Carbon dot reduced Cu_2O nanohybrid/hyperbranched epoxy nanocomposite: mechanical, thermal and photocatalytic activity. *RSC Advances*, 4(102):58453-58459, 2014.

[11] Rahman, Q. I., Ahmad, M., Misra, S. K., and Lohani, M. Effective photocatalytic degradation of rhodamine B dye by ZnO nanoparticles. *Materials Letters*, 91**:**170-174, 2013.

[12] Shahrezaei, F., Mansouri, Y., Zinatizadeh, A. A. L., and Akhbari, A. Photocatalytic degradation of aniline using TiO_2 nanoparticles in a vertical circulating photocatalytic reactor. *International Journal of Photoenergy*, 2012:430638, 2012.

[13] Thakur, S. and Karak, N. Bio-based tough hyperbranched polyurethane-graphene oxide nanocomposites as advanced shape memory materials. *RSC Advances*, 3(24):9476-9482, 2013.

[14] Sahu, S., Behera, B., Maiti, T. M., and Mohapatra, S. Simple one-step synthesis of highly luminescent carbon dots from orange juice: application as excellent bio-imaging agents. *Chemical Communications*, 48(70):8835-37, 2012.

[15] Jiang, X. C., Chen, C. Y., Chen, W. M., and Yu A. B. Role of citric acid in the formation of silver nanoplates through a synergistic reduction approach. *Langmuir,* 26(6):4400-4408, 2010.

[16] Dutta, S., Ray, C., Sarkar, S., Pradhan, M., Negishi, Y., and Pal, T. Silver nanoparticle decorated reduced graphene oxide (rGO) nanosheet: a platform for SERS based low-level detection of uranyl ion. *ACS Applied Materials & Interfaces,* 5(17):8724-8732, 2013.

[17] Thakur, S. and Karak, N. Green reduction of graphene oxide by aqueous phytoextracts. *Carbon*, 50(14):5331-5339, 2012.

[18] Wang, Y., Shi, Z., and Yin, J. Facile synthesis of soluble graphene via a green reduction of graphene oxide in tea solution and its biocomposites. *ACS Applied Materials & Interfaces,* 3(4):1127-1133, 2011.

[19] Cui, P., Lee, J., Hwang, E., and Lee, H. One-pot reduction of graphene oxide at subzero temperatures. *Chemical Communications*, 47(45):12370-12372, 2011.

[20] Michael, R. J. V., Sambandam, B., Muthukumar, T., Umapathy, M. J., and Manoharan, P. T. Spectroscopic dimensions of silver nanoparticles and clusters in ZnO matrix and their role in bioinspired antifouling and photocatalysis. *Physical Chemistry Chemical Physics*, 16(18):8541-8555, 2014.

[21] Thakur, S. and N. Karak, Multi-stimuli responsive smart elastomeric hyperbranched polyurethane/reduced graphene oxide nanocomposites. *Journal of Materials Chemistry*, 2(36):14867-14875, 2014.

[22] Deka, H., Karak, N., Kalita, R. D., and Buragohain, A. K. Bio-based thermostable, biodegradable and biocompatible hyperbranched polyurethane/Ag

nanocomposites with antimicrobial activity. *Polymer Degradation and Stability*, 95(9):1509-1517, 2010.

[23] Gurunathan, S., Han, J. W., Eppakayala, V., and Kim, J. H. Green synthesis of graphene and its cytotoxic effects in human breast cancer cells. *International Journal of Nanomedicine*, 8:1015-1027, 2013.

[24] Gurunathan, S., Han, J. W., and Kim, J. H. Green chemistry approach for the synthesis of biocompatible graphene. *International Journal of Nanomedicine*, 8:2719-2732, 2013.

[25] Song, J. and Kim, B. Rapid biological synthesis of silver nanoparticles using plant leaf extracts. *Bioprocess and Biosystems Engineering,* 32(1):79-84, 2009.

[26] Yadav, S. K., Mahapatra, S. S., and Cho, J. W. Synthesis of mechanically robust antimicrobial nanocomposites by click coupling of hyperbranched polyurethane and carbon nanotubes. *Polymer*, 53(10):2023-2031, 2012.

[27] Cai, D., Jin, J., Yusoh, K., Rafiq, R., and Song, M. High performance polyurethane/functionalized graphene nanocomposites with improved mechanical and thermal properties. *Composites Science and Technology*, 72(6):702-707, 2012.

[28] Layek, R. K., Kundu, A., and Nandi, A. K. High-performance nanocomposites of sodium carboxymethylcellulose and graphene oxide. *Macromolecular Materials & Engineering*, 298(11):1166-1175, 2016.

[29] Jeong, E. H., Yang, J., Lee, H. S., Seo, S. W., Baik, D. H., Kim, J., and Youk, J. H. Effective preparation and characterization of montmorillonite/poly(ε-caprolactone)-based polyurethane nanocomposites. *Journal of Applied Polymer Science*, 107(2):803-809, 2008.

[30] Mai, J. H., Zhang, M. Q., Rong, M. Z., Bárány, T., and Ruan, W. H. Crystallization behavior and mechanical properties of nano- $CaCO_3$/β-nucleated ethylene-propylene random copolymer composites. *Express Polymer Letters*, 6(9):739-749, 2012.

[31] Thakur, S. and Karak, N. A tough, smart elastomeric bio-based hyperbranched polyurethane nanocomposite. *New Journal of Chemistry*, 39(3):2146-54, 2015.

[32] Zhao, X. C., Zhang, Z. M., Wang, L.Y., Xi, K., Cao, Q. Q., Wang, D. H., Yang, Y., and Y. Du, Excellent microwave absorption property of graphene-coated Fe nanocomposites. *Scientific Reports*, 3:3421, 2013.

[33] Zhang, J. T., Xiong, Z. G., and Zhao, X. S. Graphene-metal-oxide composites for the degradation of dyes under visible light irradiation. *Journal of Materials Chemistry*, 21(11):3634-3640, 2011.

[34] Kaniyankandy, S., Rawalekar, S., and Ghosh, H. N. Ultrafast charge transfer dynamics in photoexcited CdTe quantum dot decorated on graphene. *Journal of Physical Chemistry C*, 116(30):16271-16275, 2012.

[35] Pirsaheb, M., Shahmoradi, B., Beikmohammadi, M., Azizi, E., Hossini, H., and Ashraf, M. M. Photocatalytic degradation of aniline from aqueous solutions under sunlight illumination using immobilized Cr:ZnO nanoparticles. *Scientific Reports,* 7(1):1473, 2017.